A two-phase fluid model for epidemic flow

Ziqiang Cheng [a], Jin Wang [b, *]

[a] *School of Mathematics, Hefei University of Technology, Hefei, Anhui, 230009, China*
[b] *Department of Mathematics, University of Tennessee at Chattanooga, Chattanooga, TN, 37403, USA*

ARTICLE INFO

ABSTRACT

We propose a new mathematical and computational modeling framework that incorporates fluid dynamics to study the spatial spread of infectious diseases. We model the susceptible and infected populations as two inviscid fluids which interact with each other. Their motion at the macroscopic level characterizes the progression and spread of the epidemic. To implement the two-phase flow model, we employ high-order numerical methods from computational fluid dynamics. We apply this model to simulate the COVID-19 outbreaks in the city of Wuhan in China and the state of Tennessee in the US. Our modeling and simulation framework allows us to conduct a detailed investigation into the complex spatiotemporal dynamics related to the transmission and spread of COVID-19.

© 2023 The Authors. Publishing services by Elsevier B.V. on behalf of KeAi Communications Co. Ltd. This is an open access article under the CC BY-NC-ND license (http://creativecommons.org/licenses/by-nc-nd/4.0/).

1. Introduction

Although mathematical and computational models have tremendously advanced our understanding in epidemiology, an accurate prediction of the spatial spread of infectious diseases still remains a challenge. Standard compartmental epidemic models based on ordinary differential equations (ODEs) are not able to incorporate spatial dynamics. To overcome this limitation, meta-population models (such as multi-patch and multi-group models) are developed to represent spatial heterogeneities and variations (Arino & van den Driessche, 2003; Cosner et al., 2009; Hanski, 1999; Hsieh, van den Driessche, & Wang, 2007; Levins, 1969; Rodriguez & Torres-Sorando, 2001; Ruan, Wang, & Levin, 2006). Such models, however, typically involve a large number of parameters, and estimating these parameters and determining their identifiability could be highly nontrivial. Another common modeling approach is based on reaction-diffusion type partial differential equations (PDEs) (Allen, Bolker, Lou, & Nevai, 2008; Bertuzzo, Casagrandi, Gatto, Rodriguez-Iturbe, & Rinaldo, 2010; Cantrell & Cosner, 2003; Magal, Webb, & Wu, 2019; Thieme, 2009; Wang, Gao, & Wang, 2015; Wang & Zhao, 2012; Wu et al., 2008; Yang & Wang, 2020b). A drawback of these PDE models, however, is their limited applicability to practical problems, partly due to the difficulty in calibrating key parameters such as the diffusion coefficients. Additionally, most of the currently available mathematical and computational models may have difficulty in forecasting where and how an epidemic is spreading in real time.

In an effort to address this challenge, we recently proposed a new epidemic flow model (Cheng & Wang, 2022) where the infected population is represented as an inviscid fluid and its motion relative to the susceptible population characterizes the

---

spatial spread of an epidemic. This model was inspired by prior modeling studies on traffic flow where the movement of vehicles is treated as an inviscid flow and described by the Euler equation (Newell, 1993; Sun, Lv, & Waller, 2011; Zhang, 1999). The present paper is a significant extension of the model in (Cheng & Wang, 2022), which contains only a single fluid, to a two-phase fluid system for a more accurate investigation into the spatiotemporal epidemic dynamics. We will introduce two different fluids to represent the susceptible and infected populations and study the epidemic flow through the movement and interaction of the two fluids.

At the initial time of an epidemic, the susceptible population may occupy the entire spatial domain or most of it, whereas the infected population may be concentrated in one or more small areas representing the onset location(s) of the disease outbreak. Through the movement of the human hosts and the contact between infected and susceptible individuals, more susceptible people become infected and the epidemic spreads out to larger areas. This process is modeled as the interaction between two fluids, through which the susceptible fluid is continuously transformed into the infected fluid. Consequently, the densities of the two fluids and the areas occupied by them keep changing throughout the epidemic, the details of which are described by our two-phase epidemic flow model.

As a demonstration of this new modeling framework, we apply it to the simulation of the transmission and spread of COVID-19. Although there are numerous mathematical and computational models published for COVID-19 (see (Afzal et al., 2022; Kevrekidis, Cuevas-Maraver, Drossinos, Rapti, & Kevrekidis, 2021; Kuhl, 2020; Leung, Wu, Liu, & Leung, 2020; Li, Pei, et al., 2020; Padmanabhan et al., 2021; Viguerie et al., 2021; Wang, 2020) and references therein), these models have not met our expectation in accurately predicting the progression and spatial spread of the disease. To address this limitation, we perform a computationally intensive study of COVID-19 combining our new epidemic model with advanced numerical methods from computational fluid dynamics (CFD). We conduct the simulation and validate the results using real epidemic data from two places: (1) the city of Wuhan in China, the first epicenter of COVID-19; and (2) the state of Tennessee in the US. Our modeling framework makes it possible to study the detailed spatiotemporal dynamics of COVID-19 in these two different scenarios.

A primary motivation of the present study is to take advantage of the well-developed theory and computational techniques in fluid dynamics, which enjoy a long history of productivity (Batchelor, 1967; Lamb, 2006; Tannehill, Anderson, & Pletcher, 1997), to improve our understanding in epidemiology, especially in the spatial spread of epidemics. Particularly, we will employ high-order weighted essentially non-oscillatory (WENO) methods (Liu, Osher, & Chan, 1994; Shu, 1997) from CFD to accurately resolve the spatial dynamics in our modeling investigation. We will demonstrate the accuracy of these computational methods through both simple tests and realistic COVID-19 simulation.

We organize the remainder of this paper as follows. In Section 2, we present details of the formulation for our two-phase epidemic flow model. In Section 3, we conduct a linear analysis for this model in the two-dimensional space. In Section 4, we describe the numerical treatment of our CFD-based epidemic model and provide simple tests to verify the order of spatial accuracy. In Section 5, we apply the modeling framework to the COVID-19 simulation in the Chinese city of Wuhan and the US state of Tennessee and discuss the results. Finally, we conclude the paper in Section 6.

2. Model formulation

We let $s(t, \boldsymbol{X})$, $i(t, \boldsymbol{X})$ and $r(t, \boldsymbol{X})$ denote the densities of the susceptible, infected (and infectious), and recovered individuals, respectively, at time t and location $\boldsymbol{X}$. We also denote the total population density by

$$n(t, \boldsymbol{X}) = s(t, \boldsymbol{X}) + i(t, \boldsymbol{X}) + r(t, \boldsymbol{X}). \tag{2.1}$$

We focus our attention on the two-dimensional (2D) space in this study so that $\boldsymbol{X} = (x, y)$ with the horizontal coordinate x and vertical coordinate y. The functions $s(t, \boldsymbol{X})$, $i(t, \boldsymbol{X})$ and $r(t, \boldsymbol{X})$ represent the numbers of susceptible, infected, and recovered individuals per unit area. Since this study is concerned with the macroscopic behavior of the epidemic, we ignore the heterogeneity of individual characteristics and treat each individual host as having the same (averaged) mass. Consequently, $s(t, \boldsymbol{X})$, $i(t, \boldsymbol{X})$ and $r(t, \boldsymbol{X})$ may also represent the mass densities of the susceptible, infected, and recovered hosts, respectively, subject to a constant multiplication. We will use both interpretations for the 'density' in this work.

If we consider a relatively short time period for an epidemic, then the total population density $n(t, \boldsymbol{X})$ may be approximately regarded as a constant, given that the infection-induced death rate is typically low. This allows us to drop one variable, $r(t, \boldsymbol{X})$, and only study the other two: $s(t, \boldsymbol{X})$ and $i(t, \boldsymbol{X})$. Building on our prior work of epidemic flow modeling (Cheng & Wang, 2022), we now treat the susceptible and infected populations as two inviscid fluids that move, mix, and interact with each other. The density of the susceptible fluid decreases, while the density of the infected (and infectious) fluid increases, through their interaction. The fluid motion thus depicts the spatial spread of the infection. Let $\boldsymbol{V}_s(t, \boldsymbol{X})$ and $\boldsymbol{V}_i(t, \boldsymbol{X})$ denote the velocity fields of the susceptible and infected fluids, respectively. In the 2D space, each velocity consists of the horizontal and vertical components:

$$\boldsymbol{V}_s(t, \boldsymbol{X}) = (u_s(t, x, y), v_s(t, x, y)), \qquad \boldsymbol{V}_i(t, \boldsymbol{X}) = (u_i(t, x, y), v_i(t, x, y)). \tag{2.2}$$

We note again that these velocities are defined at a macroscopic level and determined by the collective behavior of the populations. They do not necessarily reflect the physical motion of individual hosts.

We now derive the governing equations for $s(t, \boldsymbol{X})$, $i(t, \boldsymbol{X})$, $\boldsymbol{V}_s(t, \boldsymbol{X})$, and $\boldsymbol{V}_i(t, \boldsymbol{X})$. If we let d be the density of a physical quantity q in a 2D velocity field $\boldsymbol{V}$, Then the generalized continuity equation (Attard, 2012; Pedlosky, 1987) states that

$$\frac{\partial d}{\partial t} + \nabla \cdot (d\boldsymbol{V}) = \sigma, \tag{2.3}$$

where $d\boldsymbol{V}$ represents the flux of q and σ is the generation of q per unit area per unit time. Applying the continuity equation (2.3) separately to the susceptible and infected fluids, we obtain

$$\frac{\partial s}{\partial t} + \nabla \cdot (s\boldsymbol{V}_s) = -\beta si$$
$$\frac{\partial i}{\partial t} + \nabla \cdot (i\boldsymbol{V}_i) = \beta si - (\gamma + \omega)i, \tag{2.4}$$

where the epidemiological parameters β, γ and ω denote the disease transmission rate, the recovery rate, and the disease-induced death rate, respectively. Equation (2.4) represents an extension of the classical SIR (susceptible-infected-recovered) epidemic model with spatial movement.

Meanwhile, the velocity fields $\boldsymbol{V}_s(t, \boldsymbol{X})$ and $\boldsymbol{V}_i(t, \boldsymbol{X})$ are described by the Euler equations (Batchelor, 1967; Lamb, 2006) from fluid dynamics:

$$s\frac{\partial \boldsymbol{V}_s}{\partial t} + s\boldsymbol{V}_s \cdot \nabla \boldsymbol{V}_s = -\nabla p_s, \tag{2.5}$$

and

$$i\frac{\partial \boldsymbol{V}_i}{\partial t} + i\boldsymbol{V}_i \cdot \nabla \boldsymbol{V}_i = -\nabla p_i. \tag{2.6}$$

Here p_s is the pressure of the susceptible fluid and p_i the pressure of the infected fluid. Each pressure is usually characterized in terms of other state variables through an equation of state (Attard, 2012; Tschoegl, 2000). In this model, we assume

$$p_s = c_s s, \tag{2.7}$$

and

$$p_i = c_i i, \tag{2.8}$$

where c_s and c_i are constants, as the equations of state to close the system. Equations (2.7) and (2.8) indicate that the motion of each fluid is driven by the gradient of the fluid density. An implication is that the epidemic would spread from high-prevalence areas to low-prevalence areas. We compare these equations with the ideal gas law (Perrot, 1998; Tannehill et al., 1997) that relates the fluid pressure p and fluid density d by

$$p = R_s T d, \tag{2.9}$$

where R_s is the specific gas constant and T is the absolute temperature. Assume that T is a constant; i.e., the temperature does not change. Then equation (2.9) is in a form similar to that of equations (2.7) and (2.8). Hence, we may think of susceptible and infected individuals as moving 'particles' that are not subject to interparticle interactions, so that at the macroscopic level the motion of each population may be qualitatively analogous to an ideal gas flow.

Equations (2.4)–(2.8) thus constitute a two-phase flow model to describe the spread of an epidemic. Since the fluids are miscible and inviscid, the no-slip condition (typically for immiscible viscous fluids) does not apply, and the two fluids may have different velocities at the same location.

To proceed, we combine equations (2.4)–(2.6) into a single system:

$$\boldsymbol{U}_t + \boldsymbol{F}(\boldsymbol{U})_x + \boldsymbol{G}(\boldsymbol{U})_y = \boldsymbol{S}(\boldsymbol{U}), \tag{2.10}$$

with $\boldsymbol{U} = [i, iu_i, iv_i, su_s, sv_s, s]^T$, and

$$\boldsymbol{F}(\boldsymbol{U}) = \begin{pmatrix} iu_i \\ i(u_i)^2 + p_i \\ iu_iv_i \\ s(u_s)^2 + p_s \\ su_sv_s \\ su_s \end{pmatrix}, \quad \boldsymbol{G}(\boldsymbol{U}) = \begin{pmatrix} iv_i \\ iu_iv_i \\ i(v_i)^2 + p_i \\ su_sv_s \\ s(v_s)^2 + p_s \\ sv_s \end{pmatrix}, \quad \boldsymbol{S}(\boldsymbol{U}) = \begin{pmatrix} (\beta s - \gamma - \omega)i \\ (\beta s - \gamma - \omega)iu_i \\ (\beta s - \gamma - \omega)iv_i \\ -\beta siu_s \\ -\beta siv_s \\ -\beta si \end{pmatrix},$$

where $p_s = sc_s$ and $p_i = ic_i$ based on equations (2.7) and (2.8). We now write system (2.10) as

$$\frac{\partial \boldsymbol{U}}{\partial t} + \frac{\partial \boldsymbol{F}}{\partial \boldsymbol{U}} \frac{\partial \boldsymbol{U}}{\partial x} + \frac{\partial \boldsymbol{G}}{\partial \boldsymbol{U}} \frac{\partial \boldsymbol{U}}{\partial y} = \boldsymbol{S}(\boldsymbol{U}), \tag{2.11}$$

where the Jacobian matrices are given by

$$\frac{\partial \boldsymbol{F}}{\partial \boldsymbol{U}} = \begin{pmatrix} 0 & 1 & 0 & 0 & 0 & 0 \\ c_i - u_i^2 & 2u_i & 0 & 0 & 0 & 0 \\ -u_iv_i & v_i & u_i & 0 & 0 & 0 \\ 0 & 0 & 0 & 2u_s & 0 & c_s - u_s^2 \\ 0 & 0 & 0 & v_s & u_s & -u_sv_s \\ 0 & 0 & 0 & 1 & 0 & 0 \end{pmatrix}$$

and

$$\frac{\partial \boldsymbol{G}}{\partial \boldsymbol{U}} = \begin{pmatrix} 0 & 0 & 1 & 0 & 0 & 0 \\ -u_iv_i & v_i & u_i & 0 & 0 & 0 \\ c_i - v_i^2 & 0 & 2v_i & 0 & 0 & 0 \\ 0 & 0 & 0 & v_s & u_s & -u_sv_s \\ 0 & 0 & 0 & 0 & 2v_s & c_s - v_s^2 \\ 0 & 0 & 0 & 0 & 1 & 0 \end{pmatrix}.$$

It is easy to prove that for any real numbers a and b, the matrix $(a\,\partial\boldsymbol{F}/\partial\boldsymbol{U} + b\,\partial\boldsymbol{G}/\partial\boldsymbol{U})$ has six real eigenvalues:

$$au_i + bv_i, \quad -\sqrt{c_i\left(a^2 + b^2\right)} + au_i + bv_i, \quad \sqrt{c_i\left(a^2 + b^2\right)} + au_i + bv_i,$$

$$au_s + bv_s, \quad -\sqrt{c_s\left(a^2 + b^2\right)} + au_s + bv_s, \quad \sqrt{c_s\left(a^2 + b^2\right)} + au_s + bv_s,$$

and a complete set of eigenvectors. Hence, system (2.11) is hyperbolic.

3. Linear analysis

Mathematical analysis of the nonlinear system (2.10) is difficult. Nevertheless, a linear analysis of the model could provide useful insight. System (2.10) has a constant solution

$$\boldsymbol{U}_0 = [0,\ 0,\ 0,\ 0,\ 0,\ 1]^T, \tag{3.1}$$

after a rescaling of the total population density to 1. Equation (3.1) represents a homogeneous steady state of the model, with $s = s_0 = 1$, $i = i_0 = 0$, and $u_s = v_s = u_i = v_i = 0$ everywhere in the domain. This is commonly referred to as a disease-free equilibrium. We now linearize system (2.11) around the steady-state solution $\boldsymbol{U}_0$. We have

$$\frac{\partial \boldsymbol{F}}{\partial \boldsymbol{U}}(\boldsymbol{U}_0) = \frac{\partial \boldsymbol{F}}{\partial \boldsymbol{U}}\Big|_{\boldsymbol{U}=\boldsymbol{U}_0} = \begin{pmatrix} 0 & 1 & 0 & 0 & 0 & 0 \\ c_i & 0 & 0 & 0 & 0 & 0 \\ 0 & 0 & 0 & 0 & 0 & 0 \\ 0 & 0 & 0 & 0 & 0 & c_s \\ 0 & 0 & 0 & 0 & 0 & 0 \\ 0 & 0 & 0 & 1 & 0 & 0 \end{pmatrix}$$

and

$$\frac{\partial \boldsymbol{G}}{\partial \boldsymbol{U}}(\boldsymbol{U}_0) = \frac{\partial \boldsymbol{G}}{\partial \boldsymbol{U}}\Big|_{\boldsymbol{U}=\boldsymbol{U}_0} = \begin{pmatrix} 0 & 0 & 1 & 0 & 0 & 0 \\ 0 & 0 & 0 & 0 & 0 & 0 \\ c_i & 0 & 0 & 0 & 0 & 0 \\ 0 & 0 & 0 & 0 & 0 & 0 \\ 0 & 0 & 0 & 0 & 0 & c_s \\ 0 & 0 & 0 & 0 & 1 & 0 \end{pmatrix}.$$

Meanwhile, we have

$$\boldsymbol{S}(\boldsymbol{U}) \approx \boldsymbol{S}(\boldsymbol{U}_0) + \frac{\partial \boldsymbol{S}}{\partial \boldsymbol{U}}(\boldsymbol{U}_0)(\boldsymbol{U} - \boldsymbol{U}_0), \tag{3.2}$$

with $\boldsymbol{S}(\boldsymbol{U}_0) = \boldsymbol{0}$. The Jacobian matrix is

$$\frac{\partial \boldsymbol{S}}{\partial \boldsymbol{U}} = \begin{pmatrix} \beta s - \gamma - \omega & 0 & 0 & 0 & 0 & \beta i \\ 0 & \beta s - \gamma - \omega & 0 & 0 & 0 & \beta i u_i \\ 0 & 0 & \beta s - \gamma - \omega & 0 & 0 & \beta i v_i \\ -\beta s u_s & 0 & 0 & -\beta i & 0 & 0 \\ -\beta s v_s & 0 & 0 & 0 & -\beta i & 0 \\ -\beta s & 0 & 0 & 0 & 0 & -\beta i \end{pmatrix}.$$

In particular, we have

$$\frac{\partial \boldsymbol{S}}{\partial \boldsymbol{U}}(\boldsymbol{U}_0) = \begin{pmatrix} \beta - \gamma - \omega & 0 & 0 & 0 & 0 & 0 \\ 0 & \beta - \gamma - \omega & 0 & 0 & 0 & 0 \\ 0 & 0 & \beta - \gamma - \omega & 0 & 0 & 0 \\ 0 & 0 & 0 & 0 & 0 & 0 \\ 0 & 0 & 0 & 0 & 0 & 0 \\ -\beta & 0 & 0 & 0 & 0 & 0 \end{pmatrix}.$$

The linearized form of system (2.11) is then given by

$$\frac{\partial \boldsymbol{U}}{\partial t} + \frac{\partial \boldsymbol{F}}{\partial \boldsymbol{U}}(\boldsymbol{U}_0)\frac{\partial \boldsymbol{U}}{\partial x} + \frac{\partial \boldsymbol{G}}{\partial \boldsymbol{U}}(\boldsymbol{U}_0)\frac{\partial \boldsymbol{U}}{\partial y} = \frac{\partial \boldsymbol{S}}{\partial \boldsymbol{U}}(\boldsymbol{U}_0)\boldsymbol{U}, \tag{3.3}$$

where we have made a variable transformation $\boldsymbol{U} - \boldsymbol{U}_0 \to \boldsymbol{U}$. For convenience, we keep the same notation $\boldsymbol{U}$ in the linearized system (3.3), but $\boldsymbol{U}$ now represents a small perturbation to the equilibrium solution $\boldsymbol{U}_0$.

To proceed, we introduce the ansatz

$$\boldsymbol{U}(t,x,y) = \tilde{\boldsymbol{U}} e^{\lambda t} e^{j(kx+my)}, \tag{3.4}$$

where j is the imaginary unit satisfying $j^2 = -1$, and k and m are wave numbers associated with the horizontal and vertical spatial directions, respectively. Substituting (3.4) into equation (3.3), we obtain

$$\left[\lambda \boldsymbol{I} - \left(\frac{\partial \boldsymbol{S}}{\partial \boldsymbol{U}}(\boldsymbol{U}_0) - jk\frac{\partial \boldsymbol{F}}{\partial \boldsymbol{U}}(\boldsymbol{U}_0) - jm\frac{\partial \boldsymbol{G}}{\partial \boldsymbol{U}}(\boldsymbol{U}_0) \right) \right] \tilde{\boldsymbol{U}} = \boldsymbol{0}, \tag{3.5}$$

where $\boldsymbol{I}$ denotes the identity matrix. To ensure a nontrivial solution for $\tilde{\boldsymbol{U}}$, λ must be an eigenvalue of the matrix $\frac{\partial \boldsymbol{S}}{\partial \boldsymbol{U}}(\boldsymbol{U}_0) - jk\frac{\partial \boldsymbol{F}}{\partial \boldsymbol{U}}(\boldsymbol{U}_0) - jm\frac{\partial \boldsymbol{G}}{\partial \boldsymbol{U}}(\boldsymbol{U}_0)$; i.e.,

$$
\begin{pmatrix}
\beta - \gamma - \omega & -jk & -jm & 0 & 0 & 0 \\
-jkc_i & \beta - \gamma - \omega & 0 & 0 & 0 & 0 \\
-jmc_i & 0 & \beta - \gamma - \omega & 0 & 0 & 0 \\
0 & 0 & 0 & 0 & 0 & -jkc_s \\
0 & 0 & 0 & 0 & 0 & -jmc_s \\
-\beta & 0 & 0 & -jk & -jm & 0
\end{pmatrix}.
$$

The six eigenvalues associated with this matrix are

$$
\lambda_1 = \beta - \gamma - \omega, \qquad \lambda_{2,3} = (\beta - \gamma - \omega) \pm j\sqrt{k^2 + m^2} \cdot \sqrt{c_i},
$$

and

$$
\lambda_4 = 0, \qquad \lambda_{5,6} = \pm j\sqrt{k^2 + m^2} \cdot \sqrt{c_s}.
$$

The first three eigenvalues (λ_1, λ_2 and λ_3) characterize the wavefront of the infected fluid, with a bi-directional propagation speed $\sqrt{c_i}$ along the directions determined by the unit vectors $\pm\boldsymbol{\varphi}$, where $\boldsymbol{\varphi} = \left(\frac{k}{\sqrt{k^2+m^2}}, \frac{m}{\sqrt{k^2+m^2}}\right)$. The last three eigenvalues (λ_4, λ_5 and λ_6) characterize the wavefront of the susceptible fluid, with a bi-directional propagation speed $\sqrt{c_s}$ along the same directions $\pm\boldsymbol{\varphi}$. Meanwhile, we note that when $\beta - \gamma - \omega > 0$, the eigenvalues λ_1, λ_2 and λ_3 all have positive real parts, indicating that the disease-free equilibrium is unstable. Consequently, any tiny number of infection introduced into the system, which represents a small perturbation to the steady state $\boldsymbol{U}_0$, would grow away and spread out. This implies that if we define

$$
\mathcal{R}_0 = \frac{s_0 \beta}{\gamma + \omega} = \frac{\beta}{\gamma + \omega}, \tag{3.6}
$$

then $\mathcal{R}_0 > 1$ would indicate the persistence and spread of the infection. Note that $\mathcal{R}_0$ defined in equation (3.6) is the same as the basic reproduction number associated with the standard SIR model based on ordinary differential equations; i.e., system (2.4) with the spatial derivative terms removed, where $s_0 = 1$.

A simplified analysis is presented in the Appendix for a special scenario where a radial symmetry is assumed.

4. Numerical methods and tests

We now consider the original system (2.10). With the incorporation of fluid dynamics into epidemic modeling, the governing system (2.10) is strongly nonlinear and requires nontrivial computational methods from CFD. In particular, we seek to accurately resolve the spatial dynamics by using a fifth-order weighted essentially non-oscillatory (WENO) method (Liu et al., 1994; Shu, 1997). Specifically, we divide the spatial domain into uniform meshes marked by $k = 1, 2, \ldots, N_x$ in the x direction and $j = 1, 2, \ldots, N_y$ in the y direction. We denote the numerical approximation of $\boldsymbol{U}$ at the grid node (k, j) by $\boldsymbol{U}_{kj}$. We then formulate the following finite difference scheme to discretize the governing equation (2.10):

$$
\frac{d\boldsymbol{U}_{kj}}{dt} = \boldsymbol{L}_{kj}[\boldsymbol{U}] = \boldsymbol{S}(\boldsymbol{U}_{kj}) - \frac{\hat{\boldsymbol{F}}_{k+1/2, j} - \hat{\boldsymbol{F}}_{k-1/2, j}}{\Delta x} - \frac{\hat{\boldsymbol{G}}_{k, j+1/2} - \hat{\boldsymbol{G}}_{k, j-1/2}}{\Delta y}, \tag{4.1}
$$

where Δx and Δy denote the mesh size in the x and y directions, respectively, and where $k = 1, 2, \ldots, N_x$ and $j = 1, 2, \ldots, N_y$. In this equation, the numerical fluxes $\hat{\boldsymbol{F}}_{k\pm1/2, j}$ and $\hat{\boldsymbol{G}}_{k, j\pm1/2}$ in the x and y directions, respectively, are computed by the fifth-order WENO method. Interested readers are referred to (Shu, 1997) for details of constructing these numerical fluxes with the WENO technique.

For temporal discretization, we employ the third-order TVD Runge-Kutta scheme (Shu & Osher, 1988) to advance the numerical solution from the time step n to time step $n + 1$:

$$
\begin{aligned}
\boldsymbol{U}_{kj}^{(1)} &= \boldsymbol{U}_{kj}^n + \Delta t \boldsymbol{L}_{kj}[\boldsymbol{U}], \\
\boldsymbol{U}_{kj}^{(2)} &= \frac{3}{4}\boldsymbol{U}_{kj}^n + \frac{1}{4}\boldsymbol{U}_{kj}^{(1)} + \frac{1}{4}\Delta t \boldsymbol{L}_{kj}[\boldsymbol{U}^{(1)}], \\
\boldsymbol{U}_{kj}^{n+1} &= \frac{1}{3}\boldsymbol{U}_{kj}^n + \frac{2}{3}\boldsymbol{U}_{kj}^{(2)} + \frac{2}{3}\Delta t \boldsymbol{L}_{kj}[\boldsymbol{U}^{(2)}],
\end{aligned} \tag{4.2}
$$

for $1 \le k \le N_x$, $1 \le j \le N_y$, and $n = 0, 1, 2, \cdots$.

Since the spatial spread of the epidemic is our main focus, the accuracy of our numerical methods for spatial discretization is particularly important. In what follows, we verify the spatial accuracy of our numerical treatment using simple tests. For that purpose, we pick a known function $\boldsymbol{U}^*(t, x, y)$, and replace equation (2.10) by

$$\frac{\partial \boldsymbol{U}}{\partial t} + \frac{\partial \boldsymbol{F}(\boldsymbol{U})}{\partial x} + \frac{\partial \boldsymbol{G}(\boldsymbol{U})}{\partial y} - \boldsymbol{S}(\boldsymbol{U}) = \boldsymbol{E}^*, \tag{4.3}$$

where

$$\boldsymbol{E}^* = \frac{\partial \boldsymbol{U}^*}{\partial t} + \frac{\partial \boldsymbol{F}(\boldsymbol{U}^*)}{\partial x} + \frac{\partial \boldsymbol{G}(\boldsymbol{U}^*)}{\partial y} - \boldsymbol{S}(\boldsymbol{U}^*).$$

The function $\boldsymbol{U}^*$ is obviously an exact solution of equation (4.3). Our numerical methods described before can be applied to the left-hand side of equation (4.3), while the right-hand side of equation (4.3) can be computed by using the known function $\boldsymbol{U}^*$.

In our tests, we set the computational domain as a square $[-\pi, \pi] \times [-\pi, \pi]$, and assign the parameter values as $\beta = \gamma = \omega = c_s = c_i = 1$. We use a small time step size

$$\Delta t = \frac{0.6}{\max(|u_i| + \sqrt{c_i}, |u_s| + \sqrt{c_s})/\Delta x^{5/3} + \max(|v_i| + \sqrt{c_i}, |v_s| + \sqrt{c_s})/\Delta y^{5/3}}$$

to ensure numerical stability. As described before, the fifth-order WENO method is applied for spatial discretization. We run the numerical solution from $t = 0$ until $t = 0.5$, and compare with the analytical solution $\boldsymbol{U}^*$ to obtain the numerical error. Standard grid refinement studies are performed to check the order of accuracy for the numerical method.

Example 4.1. We take the following analytical solution for $\boldsymbol{U}^*$:

$$i(t, x, y) = \sin(t + x + y) + 2, \quad u_i(t, x, y) = 3, \quad v_i(t, x, y) = 3,$$

$$u_s(t, x, y) = 3, \quad v_s(t, x, y) = 3, \quad s(t, x, y) = 2 - \cos(t + x + y),$$

with a periodic boundary condition. At $t = 0.5$, the L^2 error and L^∞ error for $i(t, x, y)$ with different mesh sizes are displayed in Table 1, where N_x and N_y denote the number of points in the x and y directions, respectively. It is clear that fully fifth-order spatial accuracy is achieved as the grid is refined. The results for other variables are similar and not presented here.

Example 4.2. We now change the function $i(t, x, y)$ in Example 4.1 by incorporating an exponentially decaying factor:

$$i(t, x, y) = e^{-t}\sin(t + x + y) + 2,$$

while keeping the other components the same. The L^2 error and L^∞ error for $i(t, x, y)$ in this case are presented in Table 2. Again, we clearly observe fifth-order spatial accuracy of our numerical treatment.

5. COVID-19 simulation

We now apply our modeling framework to simulate the transmission and spread of COVID-19, as a demonstration of real-world applications. We will consider the city of Wuhan in China and the state of Tennessee in the US as two case studies.

We will simulate the initial phase of the COVID-19 outbreak within a relatively short time period in each of the two places. For simplicity, we assume that the total population density is uniform in space and time for each case; i.e., n (t, x, y) ≡Const, given that the disease-induced mortality rate is relatively low. Without loss of generality, we normalize this constant total density to 1; i.e.,

$$n(t, x, y) = 1, \tag{5.1}$$

for any time t and space location (x, y). Consequently, s (t, x, y), i (t, x, y) and r (t, x, y) can be regarded as the percentages of the susceptible, infected and recovered components, respectively, in the total population density.

Table 1
Numerical errors of i (t, x, y) in Example 4.1

$N_x \times N_y$	L^2 error	order	L^∞ error	order
10 × 10	6.49E-03		1.11E-02	
20 × 20	2.63E-04	4.63	3.83E-04	4.86
40 × 40	8.98E-06	4.87	1.43E-05	4.75
80 × 80	2.89E-07	4.97	4.57E-07	4.96
160 × 160	9.12E-09	4.99	1.44E-08	4.99
320 × 320	2.85E-010	5.00	4.51E-010	5.00

Table 2
Numerical errors of i (t, x, y) in Example 4.2

$N_x \times N_y$	L^2 error	order	L^∞ error	order
10×10	5.13E-03		7.48E-03	
20×20	2.19E-04	4.55	3.34E-04	4.48
40×40	7.56E-06	4.85	1.15E-05	4.86
80×80	2.44E-07	4.95	3.93E-07	4.86
160×160	7.69E-09	4.99	1.24E-08	4.98
320×320	2.41E-010	5.00	3.89E-010	5.00

For the simulation results, we will focus our attention on the spatiotemporal evolutions of the infected fluid i (t, x, y) and its velocity field, as these will provide essential quantitative information on the spread and progression of the epidemics.

5.1. COVID-19 in Wuhan, China

With a population about 9 million in 2020, the city of Wuhan has an urban area of 1528 square kilometers (Wikipedia: Wuhan). We approximate the shape of the city as a square with 40 km on each side, and define the corresponding spatial domain as

$$\Omega = \{(x, y) \mid -20\,\text{km} \leq x \leq 20\,\text{km}, \quad -20\,\text{km} \leq y \leq 20\,\text{km}\}. \tag{5.2}$$

The main onset location of the COVID-19 outbreak in Wuhan is commonly believed to be the Huanan Seafood Market (Li, Guan, et al., 2020). The market is within a chief administrative and commercial district (i.e., the Jianghan District) located in the central region of Wuhan city. It is reported that the market has a total floor area (including multi-storey space) of about 50,000 square meters. We assume that the lot area covered by the market is 40,000 square meters (or, 0.04 square kilometers) and represent it by a square in the center of the domain Ω:

$$\Gamma = \{(x, y) \mid -0.1\,\text{km} \leq x \leq 0.1\,\text{km}, \quad -0.1\,\text{km} \leq y \leq 0.1\,\text{km}\}. \tag{5.3}$$

We start our model simulation from January 24, 2020, immediately after the lock-down of Wuhan city ordered by the Chinese government (Li et al., 2020a, 2020b). Since that date was considered in the very beginning of the epidemic, we assume that the number of recovered individuals was sufficiently low that can be reasonably ignored. We then set the normalized initial densities as

$$i(0, x, y) = 0.05, \quad s(0, x, y) = 1 - i(0, x, y), \quad r(0, x, y) = 0, \qquad \text{for } (x, y) \in \Gamma, \tag{5.4}$$

and

$$i(0, x, y) = 10^{-4}, \quad s(0, x, y) = 1 - i(0, x, y), \quad r(0, x, y) = 0, \qquad \text{for } (x, y) \in \Omega - \Gamma. \tag{5.5}$$

We refer to (Cheng & Wang, 2022) for a detailed justification of this initial condition. The susceptible fluid and infected fluid are both assumed to be stationary initially; i.e.,

$$\boldsymbol{V}_s(0, x, y) = 0, \quad \boldsymbol{V}_i(t, x, y) = 0, \qquad (x, y) \in \Omega. \tag{5.6}$$

For the boundary conditions, a simple extrapolation (Tannehill et al., 1997) for the variables is applied on the four edges of the domain Ω.

We assume that all the model parameters (i.e, the transmission rate β, the recovery rate γ, the disease-induced death rate ω, and the pressure coefficients c_s and c_i) are constants. The first three of these are standard epidemiological parameters whose values can be found from prior COVID-19 modeling studies for Wuhan (Yang & Wang, 2020a; Zhuang & Wang, 2021): $\beta = 0.347$ per day, $\gamma = 1/15$ per day, and $\omega = 0.01$ per day. Note that the value of β has been rescaled by the total population size. The last two parameters c_s and c_i are related to fluid dynamics. Through the linear analysis in Section 3, however, we see that $\sqrt{c_s}$ and $\sqrt{c_i}$ represent the propagation speeds of the wavefronts associated with the susceptible and infected fluids, respectively. For simplicity, we assume that the susceptible and infected wavefronts move at the same speed; i.e., $c_s = c_i$.

We then estimate the value $c_s = c_i$ through a fitting to the real epidemic data. To that end, we compare the numerical result and the reported data based on the cumulative cases. From our model, the number of the cumulative cases at time t can be approximated by

$$\frac{N}{A(\Omega)}\int\limits_{\Omega} i(t,x,y)\,dxdy + \frac{N}{A(\Omega)}\int\limits_{\Omega} r(t,x,y)\,dxdy + \frac{N}{A(\Omega)}\int\limits_{0}^{t}\int\limits_{\Omega} \omega i(\tau,x,y)\,dxdy\,d\tau, \tag{5.7}$$

where N is the total population size, $A(\Omega)$ is the area of the domain Ω, and $N/A(\Omega)$ is the (unnormalized) total population density. The three integrals in equation (5.7) measure the numbers of active infections, recovered individuals, and disease-induced deaths, respectively, as of time t.

We use our model to fit the number of reported cumulative cases in Wuhan for a period of 17 days, from January 24, 2020 to February 10, 2020, corresponding to the ascending phase of the epidemic. We find that when $c_s = c_i = 2.0$, our model prediction based on equation (5.7) best fits the reported data. Fig. 1 displays this data fitting result.

Fig. 2 shows the contour plots of i (t, x, y) at several different times: day 5, day 7, day 10, and day 17. By our setting, the center of the domain has the highest concentration of infection at the initial time. We observe that at t = 5.0 (i.e., day 5), the epidemic wave has spread out from the domain center, with the outer wavefront forming a circle that has a radius around 10 km. Meanwhile, the largest value of i occurs on the outer wavefront. Due to the symmetry of our domain and initial conditions, the distribution of i (t, x, y) exhibits a radially symmetric pattern. A linear analysis in the Appendix shows that the wavefront generated by the infected fluid propagates in the positive radial direction at a constant speed $\sqrt{c_i} \approx 1.414$ km per day, which would imply a radius of 7.1 km at t = 5.0 for the outer wavefront circle. The difference between this and our simulation result reflects the impact of nonlinear dynamics where the wave speed may not be a constant in general. We also see that at t = 10.0, the outer wavefront moving along the positive radial direction has already reached the boundary of the domain. The highest infection density, however, occurs in a center region, an indication of the inner wavefront that moves along the negative radial direction. At t = 17.0, the infection density has developed a symmetric layered pattern, where the value of i decreases from the center to the boundary, due to the mixing and interaction between the infected and susceptible fluids.

Figs. 3 and 4 depict the profiles of the velocity components $u_i(t, x, y)$ and $v_i(t, x, y)$, respectively, for the infected fluid. The velocity fields at t = 5.0 and t = 7.0 clearly show an expansion from the center toward the boundary of the domain. At t = 17.0, both the horizontal and vertical velocities have developed a stripe pattern, where the bands of higher values are near the boundary and the bands of lower values are near the center of the domain. The evolution of the velocity fields appears to be consistent with that of the infection density, displayed in Fig. 2, in terms of space and time. Additionally, Fig. 5 shows the contour plots of the susceptible fluid density s (t, x, y) at day 5, day 7, day 10, and day 17, with reference to the contour plots of i (t, x, y) in Fig. 2. We again clearly observe a radial symmetry for the spatial distribution of the susceptible fluid.

5.2. COVID-19 in Tennessee, US

Located in the Southeastern US, the state of Tennessee has a total population of 6,916,897 in 2020 and covers roughly 42,000 square miles. Its shape is approximately a right-angled trapezoid, with a width (or, height) of 112 miles from north to south and two parallel bases from east to west (Wikipedia: Geography of Tennessee). The upper side (i.e., the long base) is about 440 miles long and the lower side (i.e., the short base) is about 310 miles long. We thus represent Tennessee in our computational domain as

$$\Omega = \left\{ (x,y)\,|\,0 \le y \le 112,\ 0 \le x \le 310 + \frac{130}{112}y \right\}, \tag{5.8}$$
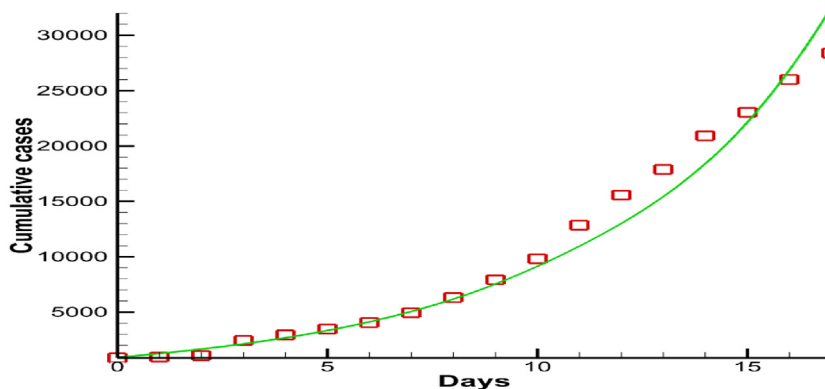

Fig. 1. Numerical simulation result (green line) versus reported data (red squares) for the cumulative COVID-19 cases in Wuhan from January 24, 2020 to February 10, 2020.
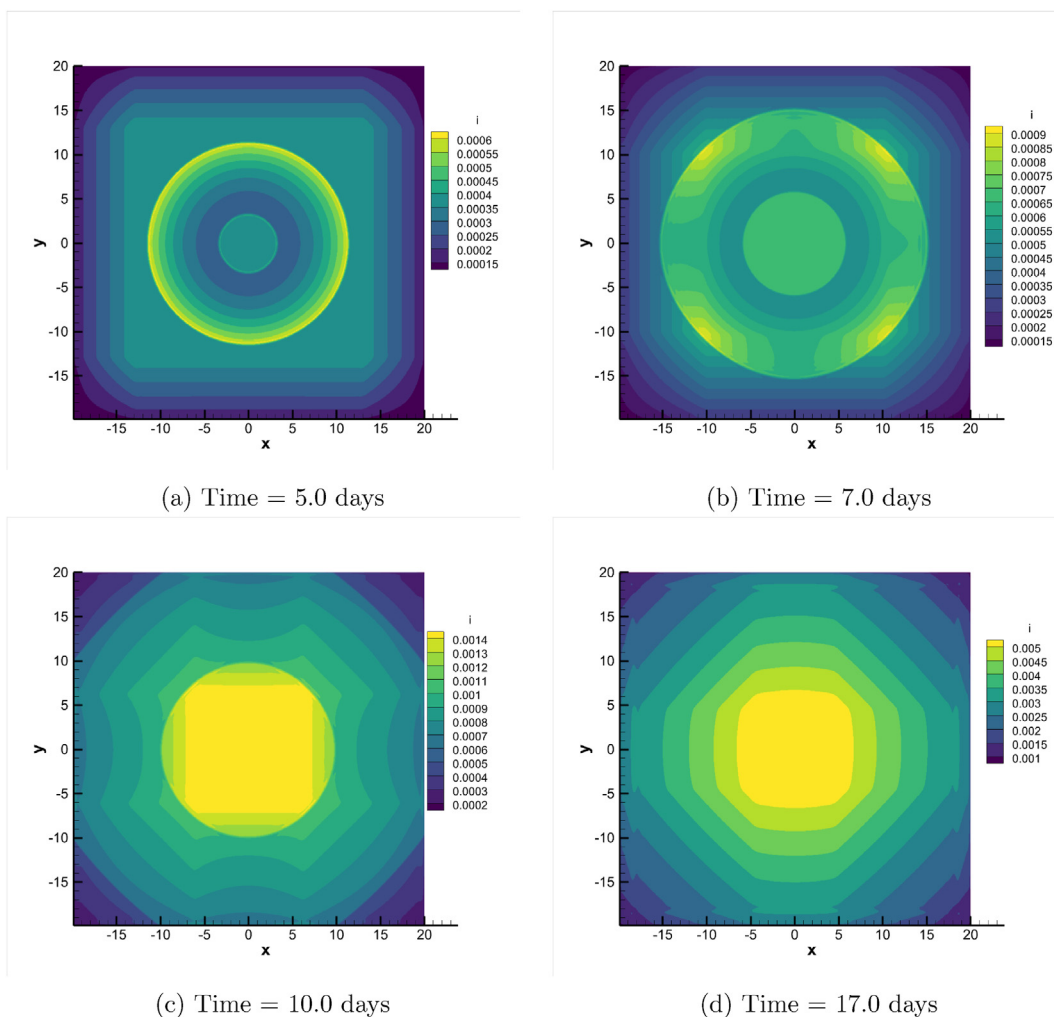
(a) Time = 5.0 days

(b) Time = 7.0 days

(c) Time = 10.0 days

(d) Time = 17.0 days

Fig. 2. Contour plots of i (t, x, y) for the COVID-19 epidemic in Wuhan.

where the length unit is mile in this domain.

Tennessee has 95 counties in total. However, about 23% of the COVID-19 cases reported in Tennessee are from the two most populous counties: Shelby and Davidson. It indicates that the epidemic is heterogeneously distributed, with cases concentrated in the most populous places. For simplicity, we represent each of the two counties by a square in our 2D setting. They are marked by SC and DC, respectively, in the computational domain Ω.

Shelby County (SC), with its county seat at Memphis which is the second-most populous city in Tennessee, has a population of 929,744 and a geographic area of 785 square miles (Wikipedia: Shelby County). Shelby County is located on the southwestern corner of Tennessee. It is represented as a square with 28 miles on each side. Davidson County (DC) has a population of 715,884 and an area of 526 square miles. Its county seat is Nashville, the state capital and largest city (Wikipedia: Davidson County). We approximate Davidson County by a square with 23 miles on each side. It is located in the northern part of the state with approximately the same distance from the east and west sides. The two subsets representing these two counties in the domain Ω are described by

$$
\begin{aligned}
SC &= \{(x, y) \mid 0 \leq x \leq 28\,\text{mi}, \ 0 \leq y \leq 28\,\text{mi}\}, \\
DC &= \{(x, y) \mid 147\,\text{mi} \leq x \leq 170\,\text{mi}, \ 68\,\text{mi} \leq y \leq 91\,\text{mi}\}.
\end{aligned}
\tag{5.9}
$$

We use the COVID-19 data reported by the Tennessee Department of Health (Tennessee Department of Health) to fit our model. We set April 2, 2020 as day 0 in our simulation. There were 2895 cumulative cases reported in the entire state of Tennessee on April 2, 2020. The two counties, Shelby and Davidson, had 653 and 694 cumulative cases, respectively. Meanwhile, on the same day the numbers of active infections were 1303 for the entire state, and 398 and 237 for Shelby and Davidson, respectively. The numbers of recovered cases were 1560 for the entire state, and 250 and 451 for Shelby and
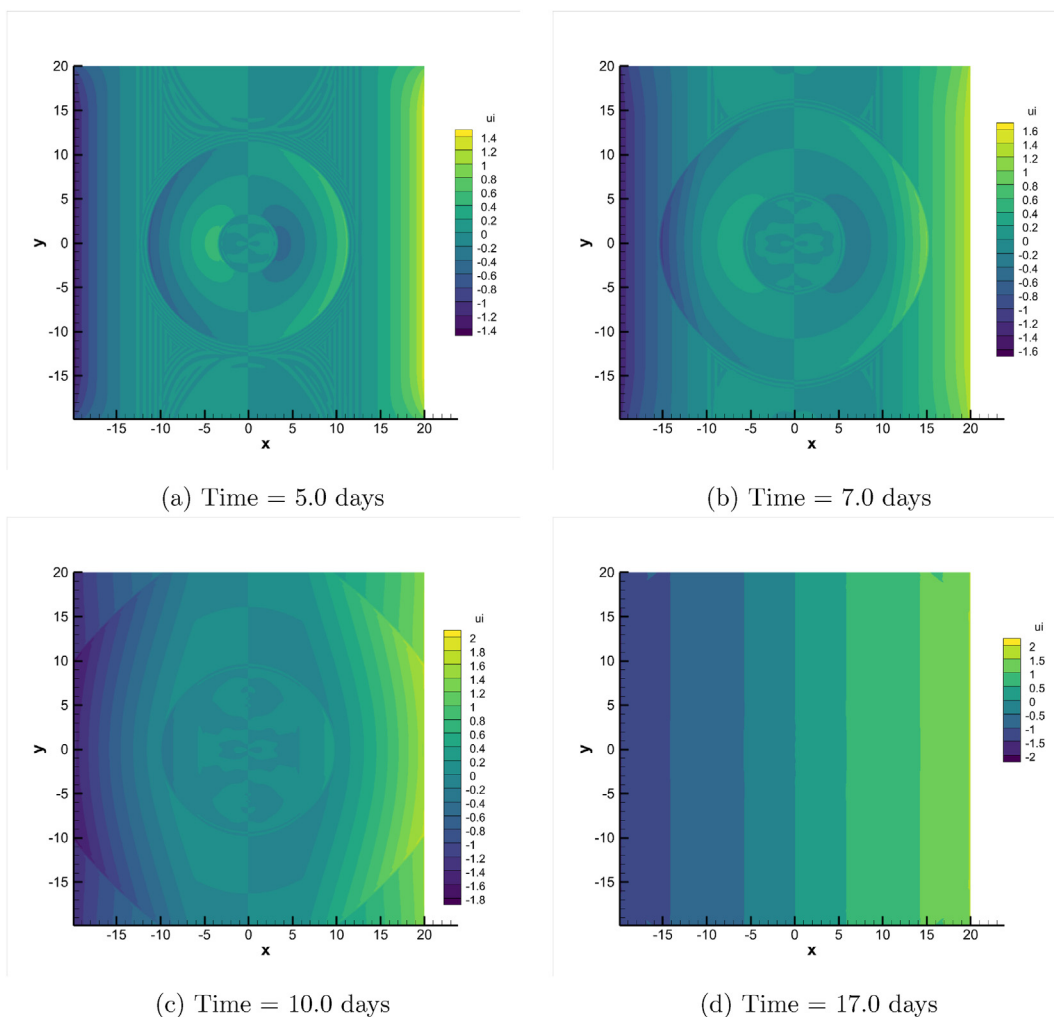
(a) Time = 5.0 days

(b) Time = 7.0 days

(c) Time = 10.0 days

(d) Time = 17.0 days

Fig. 3. Contour plots of $u_i(t, x, y)$ for the COVID-19 epidemic in Wuhan.

Davidson, respectively. Within Shelby and Davidson, we assume that the infected and recovered individuals were uniformly distributed at the initial time. The normalized initial densities for the infected fluid and the recovered population in these two counties are then given by

$$i(0, x, y) = 4.3 \times 10^{-4}, \quad r(0, x, y) = 2.7 \times 10^{-4}, \quad \text{for } (x, y) \in \text{SC};$$
$$i(0, x, y) = 3.3 \times 10^{-4}, \quad r(0, x, y) = 6.3 \times 10^{-4}, \quad \text{for } (x, y) \in \text{DC}. \tag{5.10}$$

These two counties have a total population of 1,645,628 and a combined number of 635 active cases and 701 recovered cases on April 2, 2020. The other parts of Tennessee, with a total population of 5,271,269, had a combined number of 668 active cases and 859 recovered cases at the initial time. We assume that the infected and recovered populations were uniformly distributed in the other parts of Tennessee, where the normalized initial densities for the infected fluid and recovered population are given by

$$i(0, x, y) = 1.3 \times 10^{-4}, \quad r(0, x, y) = 1.7 \times 10^{-4}, \quad \text{for } (x, y) \in \Omega - \{\text{SC, DC}\}. \tag{5.11}$$

The normalized initial density for the susceptible fluid is provided everywhere by

$$s(0, x, y) = 1 - i(0, x, y) - r(0, x, y), \quad \text{for } (x, y) \in \Omega. \tag{5.12}$$
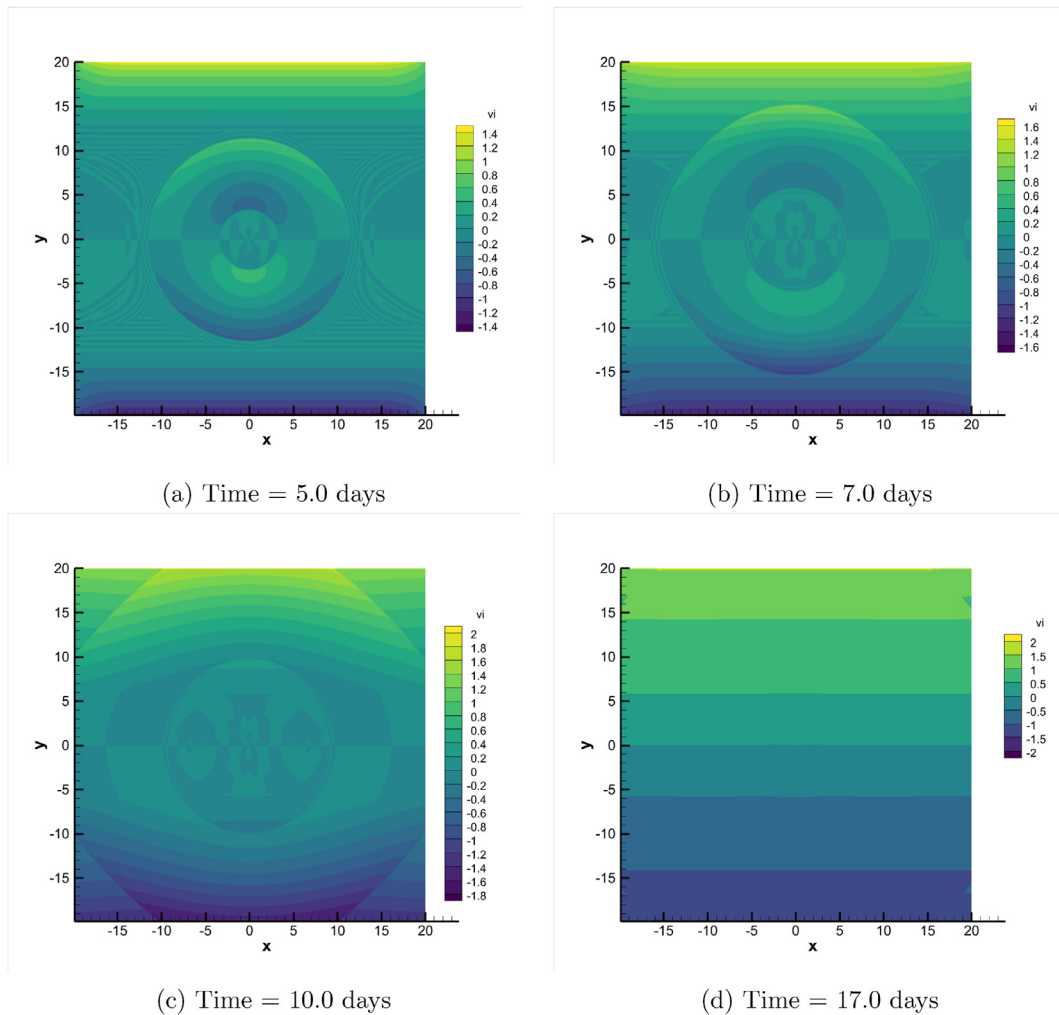
(a) Time = 5.0 days

(b) Time = 7.0 days

(c) Time = 10.0 days

(d) Time = 17.0 days

Fig. 4. Contour plots of $v_i(t, x, y)$ for the COVID-19 epidemic in Wuhan.

We clearly see that the initial infection level in Shelby County and Davidson County was much higher than the remaining parts of Tennessee. We now apply our model to simulate how the epidemic would spread out in the state, particularly, from high-prevalence areas to low-prevalence areas.

For the epidemiological parameters, we use the same values as those in Section 5.1 for the recovery rate and the disease-induced death rate: $\gamma = 1/15$ per day, and $\omega = 0.01$ per day. The disease transmission rate β typically varies from place to place. We use the transmission rate from prior modeling studies for COVID-19 in Tennessee (Yang and Wang, 2021a, 2021b), rescaled by the total population: $\beta = 0.222$ per day.

We assume $c_s = c_i$ as before. To estimate this value, we run the simulation for a period of 30 days (from April 3, 2020 to May 2, 2020) and fit the simulation result to the reported data for the cumulative cases, where the numerical calculation of the cumulative cases is again based on equation (5.7). The best fit is obtained when $c_s = c_i = 20.0$ and the fitting result is shown in Fig. 6. From the linear analysis in Section 3, we obtain that the propagation speed of the susceptible and infected wavefronts is about $\sqrt{20} \approx 4.472$ miles per day for Tennessee, which is much higher than $\sqrt{2} \approx 1.414$ kilometers per day for Wuhan. The difference could be explained by the fact that Wuhan was under a complete lockdown during the entire period of our modeling study and the movement of individuals was severely restricted, which significantly slowed down the spread of the epidemic wave. In contrast, although Tennessee also implemented timely mitigation strategies for COVID-19, they were much more lenient than those extremely strong control measures implemented in Wuhan. This, under a linear approximation, led to an epidemic propagation speed in Tennessee about 5-fold of that in Wuhan.

Fig. 7 displays the density of the infected fluid i (t, x, y) at day 0, day 5, day 10, day 20, and day 30. The panels illustrate how the epidemic spreads from the two counties, Shelby and Davidson, of high infection density in the beginning (panel a), to their neighboring places (panel b), then to areas further away from the two counties (panel c), and then to the entire state (panels
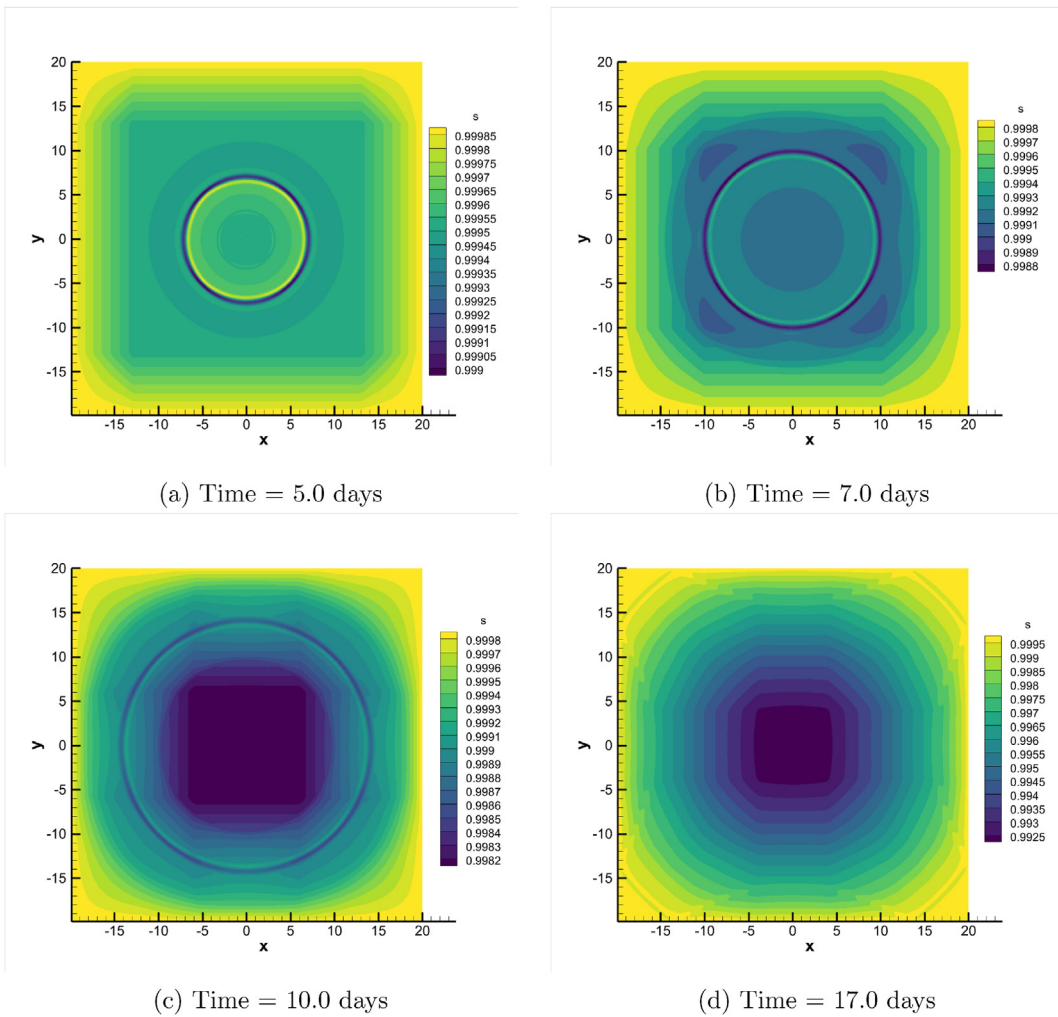
(a) Time = 5.0 days

(b) Time = 7.0 days

(c) Time = 10.0 days

(d) Time = 17.0 days

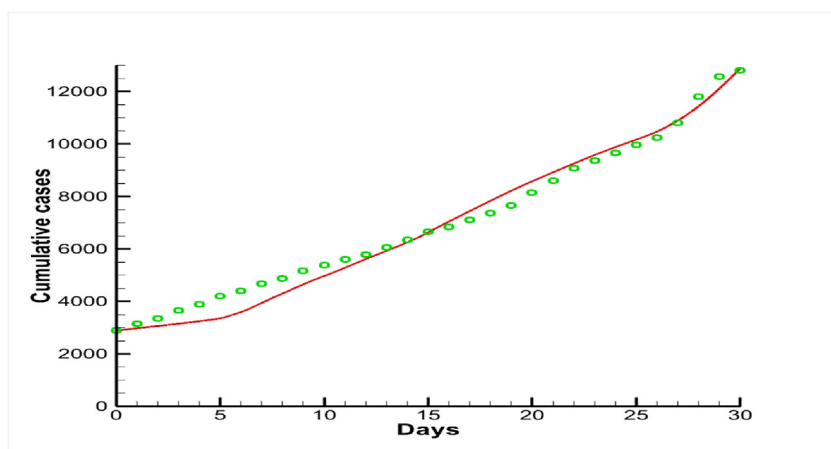**Fig. 5.** Contour plots of s (t, x, y) for the COVID-19 epidemic in Wuhan.

Fig. 6. Numerical simulation result (red line) versus reported data (green circles) for the cumulative COVID-19 cases in Tennessee from April 2, 2020 to May 2, 2020.
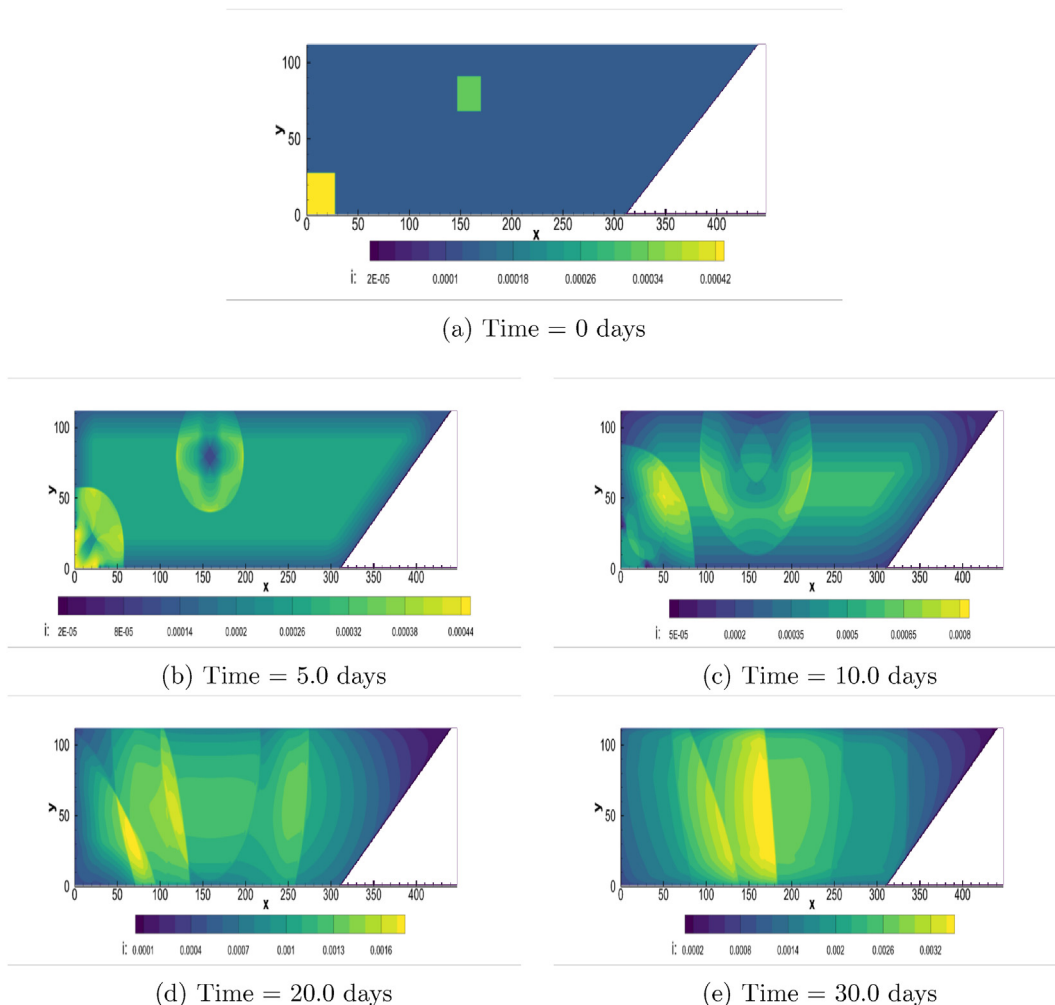
(a) Time = 0 days

(b) Time = 5.0 days

(c) Time = 10.0 days

(d) Time = 20.0 days

(e) Time = 30.0 days

Fig. 7. Contour plots of i (t, x, y) for the COVID-19 epidemic in Tennessee.

d and e). The spatial spread and distribution of the infection show a non-symmetric pattern, which is in contrast to the radial symmetry exhibited by the Wuhan simulation results. Fig. 8 displays the spatiotemporal evolution of the susceptible fluid density s (t, x, y), also in a non-symmetric manner. Meanwhile, Figs. 9 and 10 show the profiles of the velocity field, which includes the horizontal component u_i(t, x, y) and the vertical component v_i(t, x, y), at different times. These are consistent with the pattern of the infection spread depicted in Fig. 7.

5.3. Discussion on simulation results

Our modeling and computation for the COVID-19 outbreaks in Wuhan and Tennessee have focused on the ascending phase of the epidemic for each place. The Wuhan simulation represents a scenario with a radial symmetry for the disease spread, whereas the Tennessee simulation represents a non-symmetric scenario for the progression and spread of the epidemic. Our model outputs are able to match the reported data of the cumulative cases with a good accuracy in each of these case studies. More importantly, our model generates detailed predictions on the spatial distributions of the infection levels at any time, as well as the velocity profiles of the epidemic waves at any location, throughout the course of the epidemic. These results provide useful information regarding where and how fast the disease is spreading, which is important for the design of effective prevention and intervention strategies. Furthermore, the simulation outcome can be used to compare the disease risk at different spatial areas in terms of both the current situation and potential future development, so that public health administrations could effectively manage the epidemic and strategically scale resources and efforts for different locations. Our modeling framework thus can offer new insight and useful information, which may be difficult to obtain from most (if not all) of currently existing epidemic models, on the spatial dynamics of infectious diseases, particularly COVID-19.
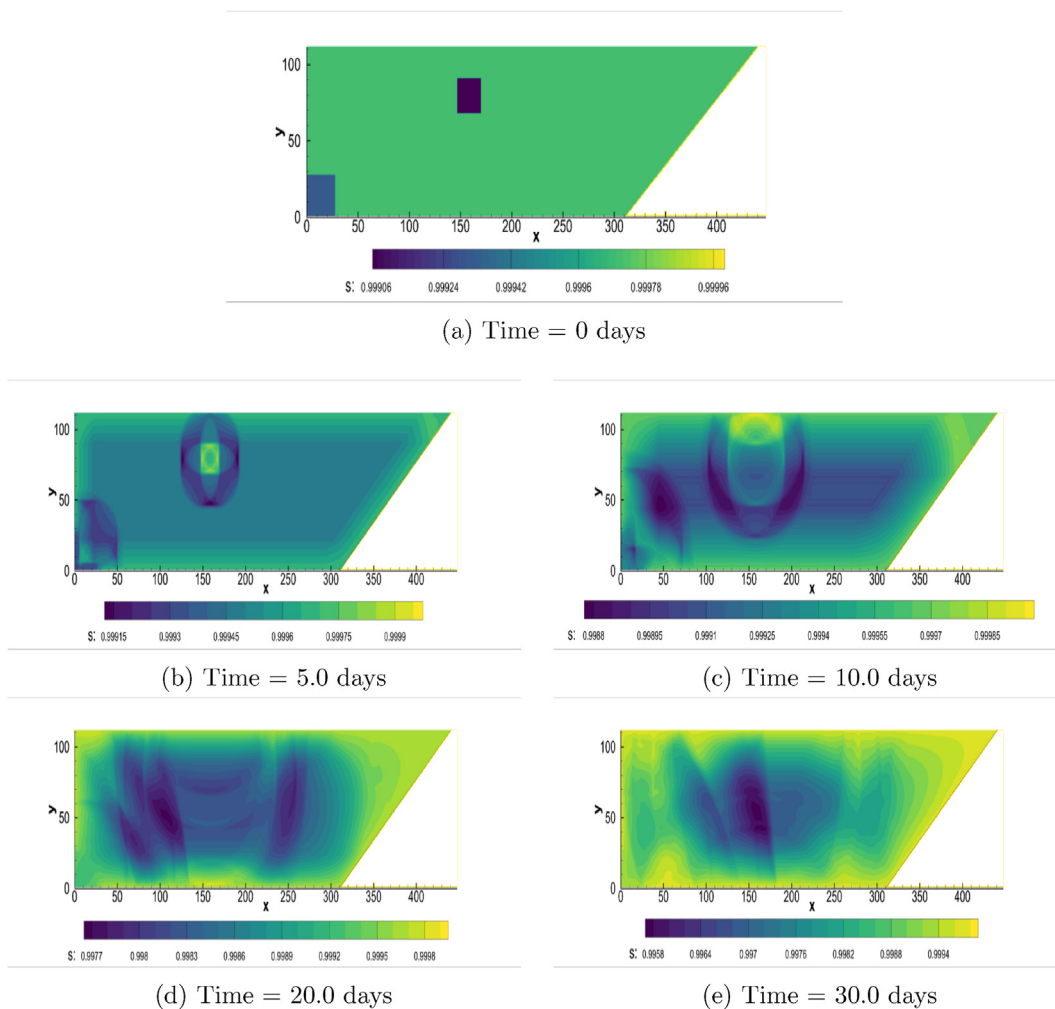
(a) Time = 0 days

(b) Time = 5.0 days

(c) Time = 10.0 days

(d) Time = 20.0 days

(e) Time = 30.0 days

Fig. 8. Contour plots of s (t, x, y) for the COVID-19 epidemic in Tennessee.

We also mention a few limitations in our COVID-19 simulation. To facilitate model implementation, we have utilized relatively simple spatial domains for Wuhan and Tennessee. We have also made simplifying assumptions on the initial distribution of population densities and infection levels. These modeling issues can be improved with more detailed data, when available, on the demography, geography, and epidemiology for each place. We have assumed that all the model parameters are constants, though in practical scenarios these parameters likely vary with time and space. The parameter values used in our simulation thus should be regarded as an average of their possible temporal and spatial variations. In addition, our PDE model is developed from the basic SIR model, and factors such as the latency period and asymptomatic infection are not considered. We can include additional compartments to account for such complications, and our epidemic flow model can be extended to accommodate more sophisticated settings.

6. Conclusions

We have proposed a two-phase fluid model to study the spatial spread of infectious diseases. This is an effort toward partially filling the knowledge gap between the complexity of epidemic spreading and the limited insight from currently available mathematical and computational models. Our new modeling framework allows us to investigate the details regarding when, where and how a real epidemic would spread. An essential feature of this modeling framework is to incorporate fluid dynamics into epidemic flow modeling and represent the susceptible and infected populations as two inviscid fluids whose motion characterizes the spatial spread of the epidemic. Through the use of a fifth-order WENO scheme, we are able to accurately compute the spatial dynamics described by our model.

The COVID-19 simulation illustrates a real-world application of our model. We have implemented and validated our model for the COVID-19 epidemics in Wuhan, China and Tennessee, US. The different spreading patterns in these two scenarios,
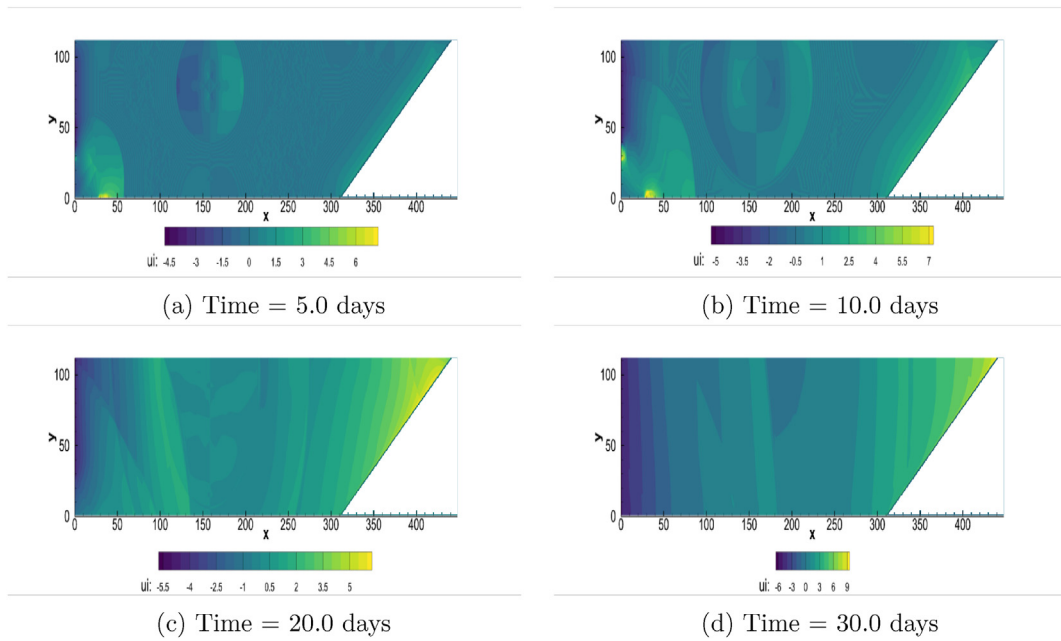
(a) Time = 5.0 days

(b) Time = 10.0 days

(c) Time = 20.0 days

(d) Time = 30.0 days

Fig. 9. Contour plots of $u_i(t, x, y)$ for the COVID-19 epidemic in Tennessee.

(a) Time = 5.0 days

(b) Time = 10.0 days

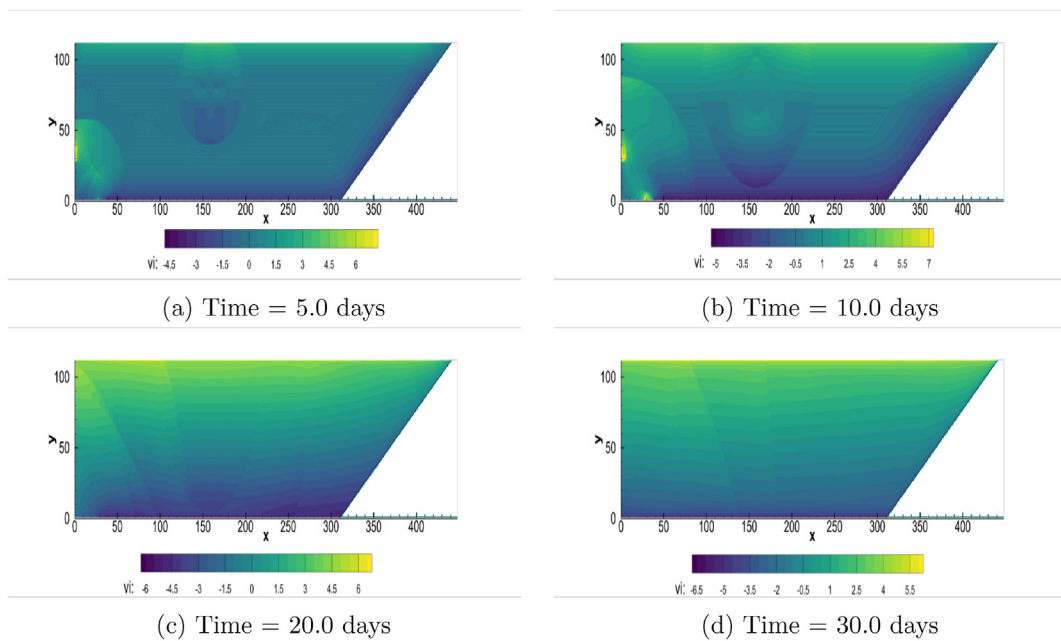(c) Time = 20.0 days

(d) Time = 30.0 days

Fig. 10. Contour plots of $v_i(t, x, y)$ for the COVID-19 epidemic in Tennessee.

generated by our simulation, highlight the complex nature of COVID-19 under different population and environmental settings and demonstrate the applicability of our modeling approach.

Our current model, based on the Euler equation from fluid dynamics, represents the motion of the susceptible and infected populations as a convection process at the macroscopic level. We may additionally incorporate the effects of randomness in human movement by introducing a diffusion process, thus extending the Euler equation to the Navier-Stokes equation, to model the epidemic flow. This could be an interesting direction for our future research.

Appendix. Radial symmetry

If we assume that the dynamical behavior of our model is radially symmetric, then the formulation and analysis could be simplified. For this special case, the infection would spread to all directions with an equal probability and with the same speed. Thus, the variables will only depend on the time, t, and the radial coordinate, ρ. We let $V_s(t, \rho)$ and $V_i(t, \rho)$ denote the radial velocities for the infected and susceptible fluids, respectively.

With the coordinate transformation $(t, x, y) \to (t, \rho)$ and the assumption of radial symmetry, equations (2.4)–(2.6) become

$$
\begin{aligned}
\frac{\partial s}{\partial t} + \frac{1}{\rho}\frac{\partial}{\partial \rho}(\rho s V_s) &= -\beta si, \\
s\frac{\partial V_s}{\partial t} + sV_s\frac{\partial V_s}{\partial \rho} &= -c_s\frac{\partial s}{\partial \rho}, \\
\frac{\partial i}{\partial t} + \frac{1}{\rho}\frac{\partial}{\partial \rho}(\rho i V_i) &= \beta si - (\gamma + \omega)i, \\
i\frac{\partial V_i}{\partial t} + iV_i\frac{\partial V_i}{\partial \rho} &= -c_i\frac{\partial i}{\partial \rho},
\end{aligned}
\tag{A.1}
$$

where we have incorporated equations (2.7) and (2.8).

If we define $\boldsymbol{U} = [i, iV_i, sV_s, s]^T$, we may also write system (A.1) in a vector form

$$
\frac{\partial}{\partial t}\boldsymbol{U} + \frac{\partial}{\partial \rho}\boldsymbol{F}(\boldsymbol{U}) = \boldsymbol{S}(\boldsymbol{U}),
\tag{A.2}
$$

with

$$
\boldsymbol{F}(\boldsymbol{U}) = \begin{pmatrix} iV_i \\ i(V_i)^2 + c_i i \\ s(V_s)^2 + c_s s \\ sV_s \end{pmatrix}, \qquad
\boldsymbol{S}(\boldsymbol{U}) = \begin{pmatrix} (\beta s - \gamma - \omega)i - iV_i/\rho \\ (\beta s - \gamma - \omega)iV_i - i(V_i)^2\big/\rho \\ -\beta siV_s - s(V_s)^2\big/\rho \\ -\beta si - sV_s/\rho \end{pmatrix}.
$$

Again, consider the disease-free equilibrium $\boldsymbol{U}_0 = [0, 0, 0, 1]^T$ of system (A.2). A linearization around the constant solution $\boldsymbol{U}_0$ and a change of variable $\boldsymbol{U} - \boldsymbol{U}_0 \to \boldsymbol{U}$ yield

$$
\frac{\partial \boldsymbol{U}}{\partial t} + \frac{\partial \boldsymbol{F}}{\partial \boldsymbol{U}}(\boldsymbol{U}_0)\frac{\partial \boldsymbol{U}}{\partial \rho} = \frac{\partial \boldsymbol{S}}{\partial \boldsymbol{U}}(\boldsymbol{U}_0)\boldsymbol{U},
\tag{A.3}
$$

where condition $\boldsymbol{S}(\boldsymbol{U}_0) = 0$ has been used. A substitution of the ansatz $\boldsymbol{U}(t,\rho) = \tilde{\boldsymbol{U}}e^{\lambda t}e^{jk\rho}$, where j is the imaginary unit and k is the wave number associated with the radial direction, then leads to an eigenvalue problem

$$
\left[\lambda \boldsymbol{I} - \left(\frac{\partial \boldsymbol{S}}{\partial \boldsymbol{U}}(\boldsymbol{U}_0) - jk\frac{\partial \boldsymbol{F}}{\partial \boldsymbol{U}}(\boldsymbol{U}_0)\right)\right]\tilde{\boldsymbol{U}} = \boldsymbol{0},
\tag{A.4}
$$

where

$$\frac{\partial \mathbf{S}}{\partial \mathbf{U}}(\mathbf{U}_0) - jk \frac{\partial \mathbf{F}}{\partial \mathbf{U}}(\mathbf{U}_0) = \begin{pmatrix} \beta - \gamma - \omega & -jk - 1/\rho & 0 & 0 \\ -jkc_i & \beta - \gamma - \omega & 0 & 0 \\ 0 & 0 & 0 & -jkc_s \\ -\beta & 0 & -jk - 1/\rho & 0 \end{pmatrix}.$$

The four eigenvalues associated with this matrix satisfy

$$\left[\lambda_{1,2} - (\beta - \gamma - \omega) \right]^2 = \frac{jkc_i}{\rho} - k^2 c_i$$

and

$$(\lambda_{3,4})^2 = \frac{jkc_s}{\rho} - k^2 c_s.$$

Consider a location that is relatively far from the origin; i.e., ρ is relatively large. Then we have

$$\lambda_{1,2} \approx (\beta - \gamma - \omega) \pm jk\sqrt{c_i} \qquad \text{and} \qquad \lambda_{3,4} \approx \pm jk\sqrt{c_s}.$$

We observe that the wavefronts of the susceptible and infected fluids move approximately at the speeds of $\sqrt{c_s}$ and $\sqrt{c_i}$, respectively, along the (positive and negative) radial directions. Meanwhile, the condition $\beta - \gamma - \omega > 0$, or $\mathcal{R}_0 > 1$ with $\mathcal{R}_0$ defined in equation (3.6), would indicate the instability of the disease-free equilibrium. These results are consistent with our findings in Section 3.

References

Afzal, A., Saleel, C. A., Bhattacharyya, S., Satish, N., Samuel, O. D., & Badruddin, I. A. (2022). Merits and limitations of mathematical modeling and computational simulations in mitigation of COVID-19 pandemic: A comprehensive review. *Archives of Computational Methods in Engineering, 29*(2), 1311–1337.

Allen, L. J. S., Bolker, B. M., Lou, Y., & Nevai, A. L. (2008). Asymptotic profiles of the steady states for an SIS epidemic reaction-diffusion model. *Discrete and Continuous Dynamical Systems, 21*, 1–20.

Arino, J., & van den Driessche, P. (2003). A multi-city epidemic model. *Mathematical Population Studies, 10*, 175–193.

Attard, P. (2012). *Non-equilibrium thermodynamics and statistical mechanics: Foundations and applications*. Oxford University Press.

Batchelor, G. K. (1967). *An introduction to fluid dynamics*. Cambridge University Press.

Bertuzzo, E., Casagrandi, R., Gatto, M., Rodriguez-Iturbe, I., & Rinaldo, A. (2010). On spatially explicit models of cholera epidemics. *Journal of the Royal Society, Interface, 7*, 321–333.

Cantrell, R. S., & Cosner, C. (2003). *Spatial ecology via reaction-diffusion equations*. Wiley.

Cheng, Z., & Wang, J. (2022). Modeling epidemic flow with fluid dynamics. *Mathematical Biosciences and Engineering, 19*(8), 8334–8360.

Cosner, C., Beier, J. C., Cantrell, R. S., Impoinvil, D., Kapitanski, L., Potts, M. D., et al. (2009). The effects of human movement on the persistence of vector-borne diseases. *Journal of Theoretical Biology, 258*, 550–560.

Hanski, I. (1999). *Metapopulation ecology*. Oxford University Press.

Hsieh, Y.-H., van den Driessche, P., & Wang, L. (2007). Impact of travel between patches for spatial spread of disease. *Bulletin of Mathematical Biology, 69*, 1355–1375.

Kevrekidis, P. G., Cuevas-Maraver, J., Drossinos, Y., Rapti, Z., & Kevrekidis, G. A. (2021). Reaction-diffusion spatial modeling of COVID-19: Greece and andalusia as case examples. *Physical Review, 104*, Article 024412.

Kuhl, E. (2020). Data-driven modeling of COVID-19 – lessons learned. *Extreme Mechanics Letters, 40*, Article 100921.

Lamb, H. (2006). *Hydrodynamics*. Cambridge University Press.

Leung, K., Wu, J. T., Liu, D., & Leung, G. M. (2020). First-wave COVID-19 transmissibility and severity in China outside hubei after control measures, and second-wave scenario planning: A modelling impact assessment. *Lancet, 395*, 1382–1393.

Levins, R. (1969). Some demographic and genetic consequences of environmental heterogeneity for biological control. *Bulletin of the Entomological Society of America, 15*(3), 237–240.

Li, Q., Guan, X., Wu, P., Wang, X., Zhou, L., Tong, Y., et al. (2020). Early transmission dynamics in Wuhan, China, of novel coronavirus-infected pneumonia. *New England Journal of Medicine, 382*, 1199. e1207.

Li, R., Pei, S., Chen, B., Song, Y., Zhang, T., Yang, W., et al. (2020). Substantial undocumented infection facilitates the rapid dissemination of novel coronavirus (SARS-CoV2). *Science, 368*, 489–493.

Liu, X., Osher, S., & Chan, T. (1994). Weighted essentially non-oscillatory schemes. *Journal of Computational Physics, 115*, 200–212.

Magal, P., Webb, G. F., & Wu, Y. (2019). On the basic reproduction number of reaction-diffusion epidemic models. *SIAM Journal on Applied Mathematics, 79*, 284–304.

Newell, G. F. (1993). A simplified theory of kinematic waves in highway traffic, part I: General theory. *Transportation Research B, 27*(4), 281–287.

Padmanabhan, R., Abed, H. S., Meskin, N., Khattab, T., Shraim, M., & Al-Hitmi, M. A. (2021). A review of mathematical model-based scenario analysis and interventions for COVID-19. *Computer Methods and Programs in Biomedicine, 209*, Article 106301.

Pedlosky, J. (1987). *Geophysical fluid dynamics*. Springer.

Perrot, P. (1998). *A to Z of thermodynamics*. Oxford University Press.

Rodriguez, D. J., & Torres-Sorando, L. (2001). Models for infectious diseases in spatially heterogeneous environments. *Bulletin of Mathematical Biology, 63*, 547–571.

Ruan, S., Wang, W., & Levin, S. A. (2006). The effect of global travel on the spread of SARS. *Mathematical Biosciences and Engineering, 3*, 205–218.

Shu, C. W. (1997). *Essentially non-oscillatory and weighted essentially non-oscillatory schemes for hyperbolic conservation laws*. Institute for Computer Applications in Science and Engineering (ICASE). Report No. 97-65.

Shu, C. W., & Osher, S. (1988). Efficient implementation of essentially non-oscillatory shock-capturing schemes. *Journal of Computational Physics, 77*(2), 439–471.

Sun, D., Lv, J., & Waller, S. (2011). In-depth analysis of traffic congestion using computational fluid dynamics (CFD) modeling method. *Journal of Modern Transportation, 19*(1), 58–67.

Tannehill, J. C., Anderson, D. A., & Pletcher, R. H. (1997). *Computational fluid mechanics and heat transfer* (2nd ed.). Taylor & Francis.

Tennessee Department of Health. Available at https://www.tn.gov/health.html.

Thieme, H. R. (2009). Spectral bound and reproduction number for infinite-dimensional population structure and time heterogeneity. *SIAM Journal on Applied Mathematics, 70*, 188–211.

Tschoegl, N. W. (2000). *Fundamentals of equilibrium and steady-state thermodynamics*. Elsevier Science.

Viguerie, A., Lorenzo, G., Auricchio, F., Baroli, D., Hughes, T. J. R., Patton, A., et al. (2021). Simulating the spread of COVID-19 via a spatially-resolved sus-ceptible-exposed-infected-recovered-deceased (SEIRD) model with heterogeneous diffusion. *Applied Mathematics Letters, 111*, Article 106617.

Wang, J. (2020). Mathematical models for COVID-19: Applications, limitations, and potentials. *Journal of Public Health and Epidemiology, 4*(9).

Wang, X., Gao, D., & Wang, J. (2015). Influence of human behavior on cholera dynamics. *Mathematical Biosciences, 267*, 41–52.

Wang, W., & Zhao, X.-Q. (2012). Basic reproduction numbers for reaction-diffusion epidemic models. *SIAM Journal on Applied Dynamical Systems, 11*, 1652–1673.

Wikipedia: Davidson County. Tennessee. Available at https://en.wikipedia.org/wiki/Davidson_County,_Tennessee.

Wikipedia: Geography of Tennessee. Available at https://en.wikipedia.org/wiki/Geography_of_Tennessee.

Wikipedia: Shelby County. Tennessee. Available at: https://en.wikipedia.org/wiki/Shelby_County,_Tennessee.

Wikipedia: Wuhan. Available at http://en.wikipedia.org/wiki/Wuhan.

Wu, J. (2008). Spatial structure: Partial differential equations models. In F. Brauer, P. van den Driessche, & J. Wu (Eds.), *Mathematical epidemiology, lecture notes in mathematics* (Vol. 1945). Springer.

Yang, C., & Wang, J. (2020a). A mathematical model for the novel coronavirus epidemic in Wuhan, China. *Mathematical Biosciences and Engineering, 17*(3), 2708–2724.

Yang, C., & Wang, J. (2020b). Basic reproduction numbers for a class of reaction-diffusion epidemic models. *Bulletin of Mathematical Biology, 82*, 111.

Yang, C., & Wang, J. (2021a). Modeling the transmission of COVID-19 in the US – a case study. *Infectious Disease Modelling, 6*, 195–211.

Yang, C., & Wang, J. (2021b). COVID-19 and underlying health conditions: A modeling investigation. *Mathematical Biosciences and Engineering, 18*(4), 3790–3812.

Zhang, H. M. (1999). Analyses of the stability and wave properties of a new continuum traffic theory. *Transportation Research B, 36*(9), 399–415.

Zhuang, Q., & Wang, J. (2021). A spatial epidemic model with a moving boundary. *Infectious Disease Modelling, 6*, 1046–1060.